Sonic hedgehog signaling in astrocytes mediates cell type-specific synaptic organization

AUTHORS: Steven Hill[1,§], Andrew Blaeser[1,§], Austin A. Coley[2], Yajun Xie[3], Katherine A. Shepard[1], Corey C. Harwell[3], Wen-Jun Gao[2], A. Denise R. Garcia[1,2*]

[1]Department of Biology, Drexel University, Philadelphia, PA 19104, USA

[2]Department of Neurobiology and Anatomy, Drexel University College of Medicine, Philadelphia, PA 19129, USA

[3]Department of Neurobiology, Harvard Medical School, Boston, MA 02115, USA

[§]Authors contributed equally to this work.

Correspondence:

A. Denise R. Garcia

Department of Biology

Department Neurobiology and Anatomy

Drexel University

3245 Chestnut St. PISB 422

Philadelphia, PA 19104

adg82@drexel.edu

Astrocytes have emerged as integral partners with neurons in regulating synapse formation and function, but the mechanisms that mediate these interactions are not well understood. Here, we show that Sonic hedgehog (Shh) signaling between neurons and astrocytes is required for establishing structural organization and remodeling of cortical synapses in a cell type-specific manner. In the postnatal cortex, Shh signaling is active in a subpopulation of mature astrocytes localized primarily in deep cortical layers. Selective disruption of Shh signaling in astrocytes produces a dramatic increase in synapse number specifically on layer V apical dendrites that emerges during adolescence and persists into adulthood. Dynamic turnover of dendritic spines is impaired in mutant mice and is accompanied by an increase in neuronal excitability and a reduction of the glial-specific, inward-rectifying K^+ channel Kir4.1. These data identify a critical role for Shh signaling in astrocyte-mediated modulation of neuronal activity required for sculpting synapses.

INTRODUCTION

The organization of synapses into the appropriate number and distribution occurs through a process of robust synapse addition followed by a period of refinement during which excess synapses are eliminated. Failure to establish or maintain appropriate synaptic organization is a hallmark of many neurodevelopmental disorders [1]. Considerable evidence now shows that, together with neurons, astrocytes are critical regulators of synaptic connectivity and function [2–4]. Astrocytes interact intimately with synapses to regulate their formation, maturation, and function, and a growing number of astrocyte-secreted proteins that directly mediate synapse formation and elimination have been identified [5–8]. Nevertheless, despite the remarkable progress in our understanding of the molecular interactions between astrocytes and synapses that facilitate synaptogenesis, the underlying signaling programs mediating astrocyte-dependent regulation of synapse organization remain poorly understood.

The molecular signaling pathway Sonic hedgehog (Shh) governs a broad array of neurodevelopmental processes in the vertebrate embryo, including morphogenesis, cell proliferation and specification, and axon pathfinding [9,10]. However, Shh activity persists in multiple cell populations in the postnatal and adult CNS, including progenitor cells, as well as in differentiated neurons and astrocytes [11–15], where novel and unexpected roles for Shh activity are emerging [16]. Following injury, Shh has been shown to mitigate inflammation [17,18], and in the cerebellum, Shh derived from Purkinje neurons instructs phenotypic properties of mature Bergmann glia [19]. In the postnatal cortex, Shh is required for establishing local circuits between two distinct projection neuron populations [14]. Shh produced by layer V neurons guides the formation of synaptic connections to its layer II/III presynaptic partners, which transduce the Shh signal through non-canonical, Gli-independent mechanisms. We have previously shown that Shh signaling is also active in a discrete subpopulation of cortical astrocytes [15], suggesting that Shh signaling mediates both homotypic and heterotypic cellular interactions. Astrocytes engaging in Shh activity are identified by expression of Gli1, a transcriptional effector of canonical Shh signaling [9]. Whether Shh signaling in cortical astrocytes plays a role in synaptic organization of neurons is not known.

In this study, we examined the organization and dynamics of dendritic spines on cortical neurons following selective disruption of Shh signaling in astrocytes. Dendritic spines are the structural hosts of most excitatory synapses and play an important role in the organization and function of neural circuits. We show that deep layer neurons exhibit long-lasting aberrations in the density and turnover of dendritic spines that emerge during postnatal development when astrocytic Shh signaling is disrupted. Notably, these perturbations in synaptic organization are not observed in upper layer neurons where Gli1 astrocytes are relatively sparse. Chronic *in vivo* imaging of dendritic spines reveals that mutant mice exhibit lower rates of spine turnover, suggesting impaired structural plasticity. In addition, these mice show a pronounced deficit in expression of the glial-specific inward-rectifying K^+ channel, Kir4.1, and concomitant hyperexcitability of cortical neurons. Taken together, these data demonstrate that astrocytes act as key modulators of neural activity and structure during postnatal development, and further establish Shh signaling as a fundamental mediator of synaptic connectivity.

RESULTS

Gli1 astrocytes exhibit a distinct laminar distribution in the adult cortex

In the mature cortex, a subpopulation of astrocytes express the transcription factor Gli1, indicating active Shh signaling [15]. Notably, the distribution of Gli1 astrocytes throughout the cortex is non-uniform, showing a laminar-specific pattern (**Figure 1**). We analyzed the laminar distribution of Gli1 astrocytes in adult *Gli1*$^{CreER/+}$;Ai14 mice, in which tamoxifen administration promotes Cre-mediated recombination of the fluorescent tdTomato reporter protein, permanently marking Gli1-expressing cells. The vast majority of marked cells were observed within layers IV and V, with few marked cells observed in layers II/III or VI (**Figure 1**). We performed immunostaining with the pan-astrocytic marker S100β and quantified the fraction of marked astrocytes in cortical layers (**Figure 1**). This analysis showed that 44% of astrocytes in layer IV express Gli1 (**Figure 1**), while 36% of astrocytes in layer V express Gli1. Interestingly, the distribution of Gli1 astrocytes in layer V was not homogenous, showing an enrichment of marked cells in layer Vb, and a distinctive paucity of marked cells in layer Va (**Figure 1**), consistent with the localization of Shh producing neurons in layer Vb [14,15]. We analyzed the fraction of Gli1 astrocytes in each sublayer of layer V and found that 75% of marked cells were found in layer Vb whereas only 25% were found in layer Va. Layers VI and II/III showed the lowest fractions of marked astrocytes, with only 11% and 22% of S100β cells expressing tomato, respectively. These data demonstrate that Gli1 astrocytes are preferentially localized in deep cortical layers and suggest their interactions with local neurons may differ from that of Gli1-negative astrocytes in superficial layers.

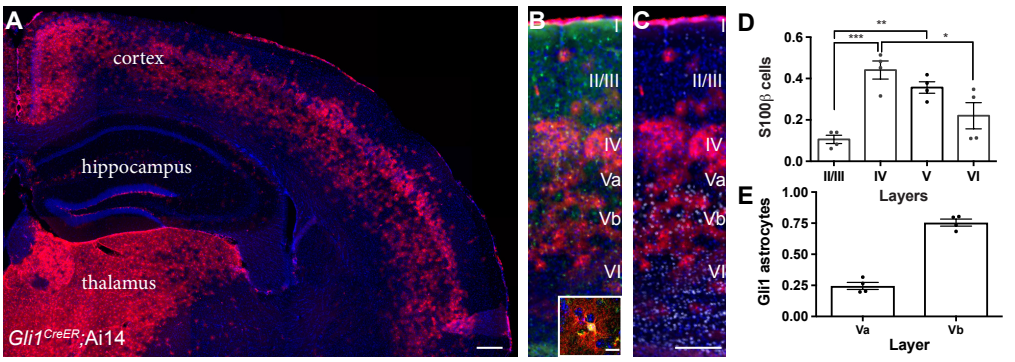

Figure 1: Gli1 astrocytes are distributed in a laminar-specific manner. (A) Tamoxifen-induced reporter expression in *Gli1*^{CreER};Ai14 mice reveals a laminar distribution of cells undergoing active Shh signaling (red). Scale bar, 250 μm. **(B)** Gli1+ cells (red) are a subset of all astrocytes (S100β, green, see inset; scale bar, 12.5 μm). **(C)** Layer analysis of Gli1 astrocytes (red) with DAPI and the deep layer marker Ctip2 (gray) illustrate their layer-specific organization. Scale bar, 125 μm. **(D)** The fraction of astrocytes expressing Gli1 in each cortical layer. Data points indicate individual animals, bars represent mean ± SEM. Statistical signficance was assessed by one-way ANOVA with Tukey's post hoc test for multiple comparisons. *, $p < 0.05$; **, $p < 0.01$; ***, $p < 0.01$. **(E)** The fraction of Gli1 astrocytes in sublayers Va and Vb. Bar graphs represent mean value ± SEM. $n = 4$ animals.

Shh signaling is required for cell type-specific synaptic connectivity

Transduction of canonical Shh signaling begins with binding of Shh to its transmembrane receptor, Patched1 (Ptch), relieving inhibition of a second, obligatory co-receptor Smoothened (Smo). To

115 investigate the role of Shh signaling in astrocyte function, we performed conditional knockout of Smo
116 selectively in astrocytes using GFAP-Cre transgenic mice in which Cre expression is regulated by the full-
117 length mouse GFAP promoter[20] (mGFAP Smo CKO). Because mGFAP-mediated Cre recombination
118 targets astrocyte progenitors expressing GFAP which are present at birth, we can effectively delete Shh
119 activity in all cortical astrocytes [21]. Nevertheless, because Shh signaling occurs in postnatal neurons, and
120 because recombination in cortical neurons has been observed in some GFAP-Cre transgenic lines[22], we
121 performed further validation of the Cre-mediated recombination pattern by crossing mGFAP-Cre mice
122 with Ai14 reporter mice (*mGFAP-Cre;*Ai14). We analyzed the identity of tdTomato-expressing cells
123 (tomato) in the somatosensory cortex of *mGFAP-Cre;*Ai14 reporter mice by immunohistochemistry with
124 cell type-specific markers (**Figure 2 – figure supplement 1**). Although individual floxed alleles possess
125 distinct recombination efficiencies, analysis of recombination in a reporter line provides a useful
126 approximation of the expression pattern of a given Cre driver. The vast majority of tomato-positive cells
127 showed a bushy morphology, typical of
128 protoplasmic astrocytes (**Figure 2 – figure**
129 **supplement 1**). Double staining with S100β
130 showed that nearly 70% of tomato-expressing
131 cells were co-labeled, identifying them as
132 astrocytes. A small fraction (9%) of tomato
133 cells were co-labeled with NeuN, identifying
134 them as neurons. Conversely, only 1.3% of
135 cortical neurons were labeled with tomato,
136 and these were localized primarily to upper
137 layers (**Figure 2 – figure supplement 1**). We
138 also identified a small fraction (6%) of tomato
139 cells as oligodendrocytes. Importantly,
140 although a minor fraction of recombined cells
141 was identified as neurons or
142 oligodendrocytes, nearly all cortical astrocytes
143 analyzed expressed the tdTomato reporter
144 protein (95%), suggesting that this mGFAP-Cre
145 driver is an effective tool for selective
146 deletion of Smo in all cortical astrocytes.

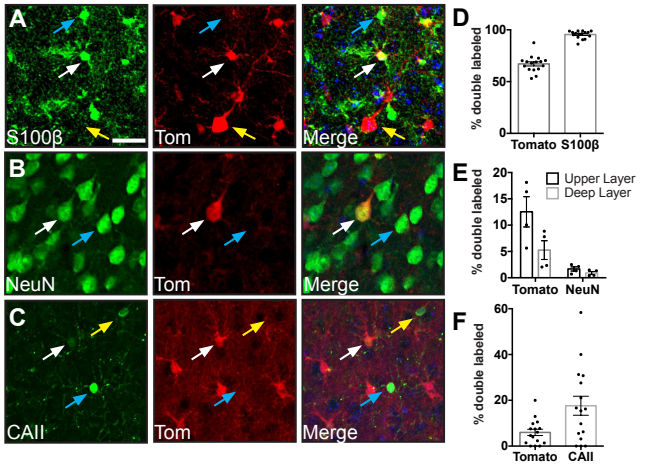

Figure 2 – Figure supplement 1: Gfap-Cre recombination occurs primarily in astrocytes. (A) Expression of the astrocyte marker S100β and tdTomato in somatosensory cortex. Scale bar, 25 µm. **(B)** Expression of the neuronal marker NeuN and tdTomato in somatosensory cortex. **(C)** Expression of the oligodendrocyte marker CAII and tdTomato in somatosensory cortex. White arrows show cells that express the indicated marker and are derived from a GFAP+ cell. Blue arrows show cells that express the indicated marker but are not derived from a GFAP+ cell. Yellow arrows show cells derived from a GFAP+ cell that does not express the given markers. **(D-F)** Fraction of recombined cells identified as astrocytes (D), neurons (E), or oligodendrocytes (F) in the cortex of adult *Gfap-Cre;*Ai14 mice. Data points represent individual brain sections analyzed. Bar graph represent mean ± SEM. *n* = 2 animals.

147

148 During postnatal development, Shh is required for establishing synaptic connectivity between layer V
149 neurons and their presynaptic partners in layer II/III, which is mediated by Gli-independent, non-
150 canonical signaling [14]. To examine whether canonical, Gli-mediated Shh signaling in astrocytes plays a
151 role in establishing synaptic connectivity of cortical neurons, we evaluated spine density of apical
152 dendrites on layer V neurons in the somatosensory cortex of mGFAP Smo CKO mice across postnatal

development. Dendritic spines receive the vast majority of excitatory input, thereby serving as a useful readout of synaptic connectivity[23]. To visualize neurons for reliable identification and tracing, mGFAP Smo CKO mice were crossed with Thy1-GFPm transgenic mice, which sparsely express GFP in a subset of layer V cortical neurons [24]. Dendritic spines undergo a period of dynamic reorganization during postnatal development during which there is an initial overproduction of spines during the first 2-3 weeks of postnatal development, followed by a period of synaptic pruning that refines the precise connectivity of cortical circuits [25]. At P14, spine density was comparable between mGFAP Smo CKO mice and wild type (WT) littermate controls, suggesting that early synaptogenesis does not require astrocytic Shh signaling (0.58 ± 0.03 spines/µm and 0.56 ± 0.01 spines/µm, WT [n = 7 cells] and mGFAP Smo CKO [n = 6 cells], respectively, p = 0.64, 2 animals per genotype). Between P14 and P21, spine density remained stable in WT, but showed a dramatic increase at P28 (**Figure 2**). This period of synapse addition was followed by a steady reduction in spine density at P42 and into adulthood (≥P90), reflecting the developmental elimination of spines. In contrast, mGFAP Smo CKO mice showed an accelerated timeline of spine addition in which spine density increased dramatically between P14 and P21 (**Figure 2**). Spine density was significantly higher at P21 in mGFAP Smo CKO mice compared to controls (0.53 ± 0.05 spines/µm and 0.76 ± 0.06 spines/µm, WT and mGFAP Smo CKO, respectively, p = 0.008, n = 9 cells from 3 animals per genotype). Although there was a modest reduction in spine density as animals matured, spine density remained elevated in adult mGFAP Smo CKO mice compared to WT controls (0.36 ± 0.02 spines/um and 0.60 ± 0.02 spines/µm in WT [n = 24 cells] and mGFAP Smo CKO [n = 23 cells], respectively, p < 0.0001, 4 animals per genotype; **Figure 2**). Thus, whereas WT mice experience a 49% reduction in spine density from the peak of spine density at P28 to adulthood, mGFAP Smo CKO mice exhibit a 22% reduction from

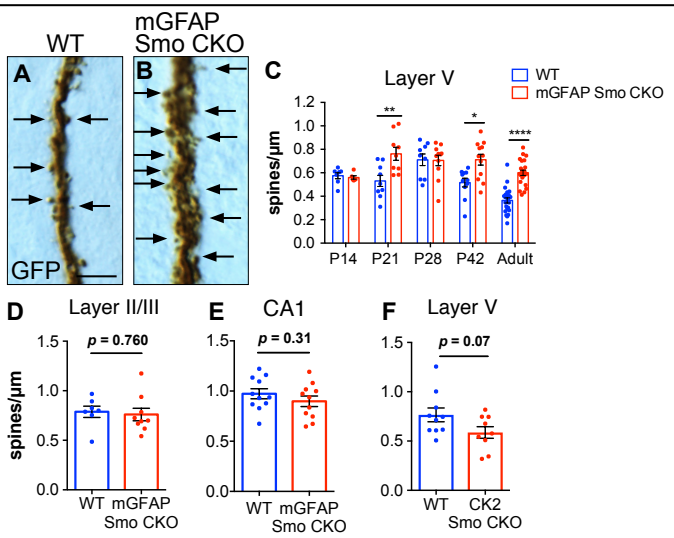

Figure 2: Loss of Shh signaling in astrocytes results in increased spine density on layer V neurons. (A-B) GFP immunostaining of representative apical dendritic segments from layer V neurons in a WT (A) and mGfap Smo CKO (B) mice at P21. Arrows indicate individual spines. Scale bar, 5 μm. (**C**) Spine density of apical dendrites from layer V neurons across various postnatal ages and in adult mice. Data points represent individual cells, bars represent mean ± SEM. Statistical analysis performed by two-way ANOVA with Tukey's post-hoc test for multiple comparisons. *, p < 0.05; **, p < 0.01; ****, p < 0.0001. Significance is stated as mGFAP Smo CKO compared to WT at a given age. (**D-E**) Spine density of apical dendrites from CA1 pyramidal neurons (D) and layer II/III (E) in WT and mGfap Smo CKO mice. (**F**) Spine density of apical dendrites from layer V neurons in adult CamKIIa Smo CKO mice. Data points represent individual cells, bars represent mean ± SEM. Statistical signfiicance assessed by Student's t-test. n ≥ 3 animals per genotype for all ages but P14, where n = 2 animals per genotype.

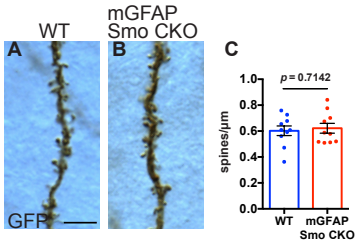

Figure 2 – figure supplement 2: Spine density on layer V basal dendrites are not affected in adult mGFAP Smo CKO mice. (A-B) Representative images of basal dendrites analyzed from layer V neurons expressing *Thy1GFPm* in both WT (*Smo*$^{fl/fl}$) and mGFAP Smo CKO (*Gfap-Smo*$^{fl/fl}$) animals. Scale bar, 5 µm. **(C)** Graph comparing the density of spines on basal dendrites from WT and mGFAP Smo CKO animals. Data points represent individual cells, bars represent mean ± SEM. Statistical significance was assessed using unpaired Student's t-test. n = 3 animals per genotype.

195 their peak at P21 to adulthood. Interestingly, we find no difference in basal dendrite spine density in
196 mGFAP Smo CKO mice (0.60 ± 0.04 spines/um and 0.62 ± 0.04 spines/µm in WT and mGFAP Smo CKO,
197 respectively, p = 0.71, n = 10 cells from 3 animals per genotype; **Figure 2 – figure supplement 1**). This is
198 in contrast to embryonic deletion of Shh from neurons using the EmxCre driver, which produces a
199 reduction in spine density of basal dendrites on layer V neurons [14]. These data suggest that while the
200 early stages of synapse formation proceed independently of astrocytic Shh signaling, the maturing
201 cortical circuit requires intact Shh activity in astrocytes for the developmental pruning of excess
202 synapses necessary to achieve its mature organization.

203

204 To confirm that elevated spine density was due specifically to a loss of astrocytic Shh signaling, we
205 interrogated the spine density of pyramidal cells in two different regions where Gli1 astrocytes are
206 relatively sparse (see **Figure 1**). Pyramidal neurons in layer II/III of WT mice showed a higher spine
207 density than layer V neurons (0.79 ± 0.06 spines/µm, n = 7 cells, 4 animals) consistent with previous
208 studies [26]. However, this was not significantly different from the spine density observed in mGFAP Smo
209 CKO mice (0.76 ± 0.06 spines/µm, p = 0.76, n = 9 cells, 5 animals; **Figure 2**). We also analyzed pyramidal
210 neurons in the hippocampus. Although the dentate gyrus of the hippocampus harbors a population of
211 Gli1-expressing adult neural progenitor cells [12,27], mature, differentiated astrocytes expressing Gli1 are
212 relatively sparse (**Figure 1**). The spine density of CA1 pyramidal neurons in adult mice was higher than in
213 cortical neurons, consistent with previous studies [28,29]. However, there was no significant difference in
214 spine density between mGFAP Smo CKO mice and WT controls (0.97 ± 0.05 spines/µm and 0.90 ± 0.05
215 spines/µm in WT and mGFAP Smo CKO, respectively, p = 0.32, n = 11 cells from 3 animals per genotype;
216 **Figure 2**). Our analysis of the recombination pattern of the mGFAP-Cre driver showed that some cortical
217 neurons undergo recombination (**Figure 2 – figure supplement 1**). To rule out the possibility that Smo
218 deletion in a small population of neurons is responsible for the elevated spine density of layer V
219 neurons, we deleted Smo in excitatory neurons using the CamKIIa Cre driver (CK2 Smo CKO), and
220 evaluated spine density of layer V neurons in adult mice. We found no significant difference in spine
221 density between CK2 Smo CKO mice and littermate controls (0.77 ± 0.07 spines/um and 0.59 ± 0.06
222 spines/um in WT [n = 10 cells] and CK2 Smo CKO [n = 9 cells], respectively, p = 0.07, 3 animals per
223 genotype; **Figure 2**). Taken together, these data suggest that Shh activity in astrocytes is necessary for
224 the developmental reorganization of dendritic spines specifically on layer V cortical neurons. Notably,
225 we observed elevated spine density along the apical dendrites of layer V neurons, which traverse layer
226 II/III, where few Gli1 astrocytes are found. This suggests that the modification of synapse organization
227 mediated by Gli1 astrocytes does not occur through direct astrocyte-synapse interactions.

228 Synapses are more stable in mGFAP Smo CKO mice

229 Dendritic spines are dynamic structures that undergo rapid formation and elimination during postnatal
230 cortical development. As cortical circuits mature, the fraction of spines undergoing dynamic turnover
231 declines concomitant with an increase in spine stability [25,26]. The dynamic turnover of spines has long
232 been considered a structural correlate of synaptic plasticity and can be regulated in an activity-
233 dependent manner [30–33]. To evaluate the role of astrocytic Shh signaling in mediating spine dynamics,
234 we performed repeated *in vivo* imaging of the apical tufts of layer V neurons in the somatosensory

cortex through a cranial window [34]. We confirmed the layer V identity of imaged neurons by following individual dendritic segments to their soma and created 3D reconstructions of imaged neurons. Only dendrites with soma in layer V, typically 500 µm – 600 µm from the surface of the brain, were analyzed. In Thy1-GFPm mice, expression of GFP is developmentally regulated such that at P14, the intensity of GFP expression and the density of fluorescently labeled neurons within the 3 mm cranial window is insufficient for reliable imaging, as has been previously reported [26]. However, by P17, GFP expression was sufficiently dense and bright to enable reliable imaging. We analyzed the fraction of spines undergoing dynamic turnover over 2 days in young mice at P17-P21 and P28-P32. In WT mice, the turnover ratio was 0.14 at P17-P21 and 0.09 in P28-P32 mice, though this was not statistically significant (p = 0.12, n = 5 mice; **Figure 3**). In mGFAP Smo CKO mice, however, the turnover ratio was lower at P17-P21 than in WT mice, and remained constant at P28-P32 (0.11 and 0.10, P17-P21 and P28-P32, respectively, n = 4 mice; **Figure 3**). This suggests that dendritic spines in mGFAP Smo CKO mice stabilize earlier than those in WT mice. Consistent with this, we found that the fraction of filopodia was lower in juvenile mGFAP Smo CKO mice compared to WT controls (**Figure 3**). Filopodia are structural precursors of dendritic spines and exhibit higher rates of dynamic turnover than mature spines [35,36]. Accordingly, the density of filopodia declines as the cortex matures [25,37]. Consistent with this, the fraction of all protrusions in juvenile WT mice identified as filopodia was 24%, but that fraction declined significantly to 15% in adults (p = 0.0016; **Figure 3**). In contrast, we did not

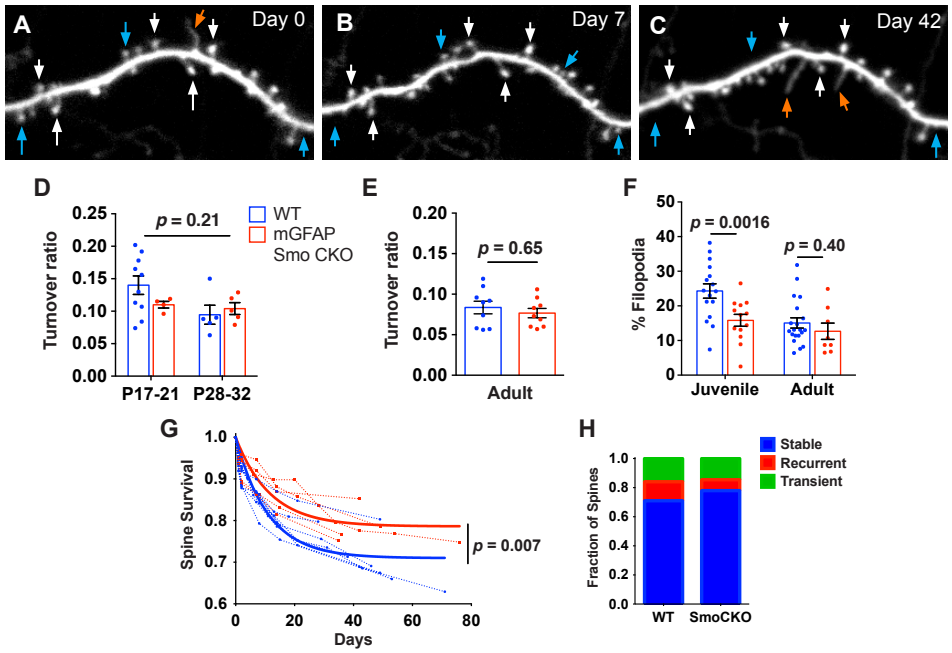

Figure 3. Loss of astrocytic Shh signaling impairs structural plasticity. (**A-C**) Example dendrite segment imaged repeatedly over 6 weeks. Day 0 indicates the first day of imaging, subsequent imaging days indicated. White arrows, stable spines; cyan arrows, transient spines; orange arrows, filopodia. (**D**) Turnover ratios in WT (n = 5 animals) and mGFAP Smo CKO (n = 4 animals) juvenile mice analyzed over 2 days. **(E)** Turnover ratios in WT (n = 6 animals) and mGFAP Smo CKO (n = 9 animals) adult mice analyzed over 7 days. Data points represent individual cells, bars represent mean ± SEM. Statistical analysis by two-way ANOVA (D) and unpaired Student's t-test (E). (**F**) Fraction of protrusions identified as filopodia in in juvenile (WT, n = 11 animals; mGFAP Smo CKO, n = 10 animals) and adult mice (WT, n = 16: mGFAP Smo CKO, n = 7 animals). Statistics by two-way ANOVA, Tukey's post hoc test. (**G**) Comparison of spine survival curves for WT and mGFAP Smo CKO neurons. Each dashed curve represents the curve from an individual mouse (WT, n = 7 animals; mGFAP Smo CKO, n = 5 animals). Solid curves represent best-fits to exponential decay models. (**H**) The fraction of spines belonging to the stable, recurrent, and transient populations. Statistical significance was assessed by Student's t-test for each class (stable, recurrent, or transient; n = 7 and 8 animals, WT and mGFAP Smo CKO, respectively). Stable, p = 0.0485; Recurrent, p = 0.1023; Transient, p = 0.7709.

observe this age-dependent decline in mGFAP Smo CKO mice (16% and 13% in juvenile and adult mGFAP Smo CKO mice, respectively). The filopodial fraction in juvenile mGFAP Smo CKO mice was already significantly below WT levels (16% vs 24% in mGFAP Smo CKO and WT mice, respectively) and similar to adult WT levels (15% and 13% in WT and mGFAP Smo CKO adult mice, respectively). It is well established that the rate of synaptic turnover declines considerably as animals mature, reflecting an increase in stability of synaptic connections [25,26]. These results indicate that disruption of Shh signaling selectively in astrocytes accelerates the stabilization of dendritic spines on layer V cortical neurons.

We next sought to investigate the long-term stability of individual spines in adult mice by imaging dendrites weekly for up to 6 weeks. We investigated the fraction of spines identified on the first day of imaging that persisted in subsequent imaging sessions and calculated the survival fraction by fitting to an exponential decay model (**Figure 3;** see Methods). This analysis revealed a larger proportion of long-lived stable spines in mGFAP Smo CKO mice compared to WT control (71% and 79% in WT [n = 7 mice] and mGFAP Smo CKO [n = 5 mice], respectively, p = 0.0068, Extra sum-of-squares F test; **Figure 3**), suggesting an increase in stability of dendritic spines. Interestingly, among the population of dynamic spines, we found two distinct populations consisting of transient spines, which disappeared and did not reappear for the duration of the study, and recurrent spines, which disappeared and then subsequently reappeared. Our data showed that the shift towards increased spine stability in the mGFAP Smo CKO neurons was entirely due to a reduction in the proportion of recurrent spines, with nearly identical fractions of transient spines observed across both genotypes (**Figure 3**). Taken together, these data suggest that structural plasticity is impaired in mGFAP Smo CKO mice. This deficit in structural plasticity emerges during the third week of postnatal development and persists into adulthood. This suggests that Shh signaling between neurons and astrocytes is required for refining synaptic connections in the cortex.

Shh signaling regulates Kir4.1 expression in cortical astrocytes

In both the developing and adult CNS, astrocytes directly eliminate synapses in an activity-dependent manner through MEGF10 and MERTK, two phagocytic receptors enriched in astrocytes [38]. To investigate whether these genes are negatively regulated in mGFAP Smo CKO mice, we examined their expression in the cortex of adult mice by quantitative PCR (qPCR). There was no difference in expression level of *Mertk* between WT and mGFAP Smo CKO mice (dCq values: 5.99 ± 0.16 and 5.83 ± 0.06 in WT [n = 4 mice] and mGFAP Smo CKO [n = 5 mice] respectively, p = 0.35; **Figure 4 – figure supplement 1).** Expression of *Megf10* showed a trend towards increased expression (dCq values: 8.13 ± 0.29 and

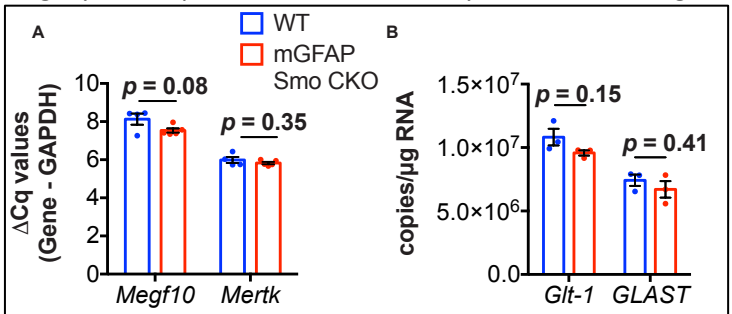

Figure 4 – figure supplement 1: Quantititive PCR analysis of known spine and synapse modulators show no change in expression in mGFAP Smo CKO mice. (A) Quantitive PCR shows a slight, but not significant, increase in *Megf10* and no change in *Mertk* in mGFAP Smo CKO animals compared to controls (n = 4 and 5 samples of cortical RNA from WT and mGFAP Smo CKO animals, respectively). Statitistical significance assessed by unpaired Student's t-test of the quantification cycles for each sample. Error bars represent standard error of the mean. **(B)** Droplet digital PCR shows no difference in the number of trancripts of either *GLT-1* or *GLAST* in mGFAP Smo CKO animals (n = 3 cortical RNA samples per genotype). Statistical significance assessed by unpaired Student's t-test of the copy number for each target in each genotype. Error bars represent standard error of the mean.

7.53 ± 0.11 in WT [*n* = 4 mice] and mGFAP Smo CKO [*n* = 5 mice], respectively; **Figure 4 – figure supplement 1**), though this difference was not statistically significant ($p = 0.075$). These data suggest that direct engulfment of synapses by astrocytes through these pathways is not regulated by Shh signaling and is not responsible for the increased spine density seen in mGFAP Smo CKO animals.

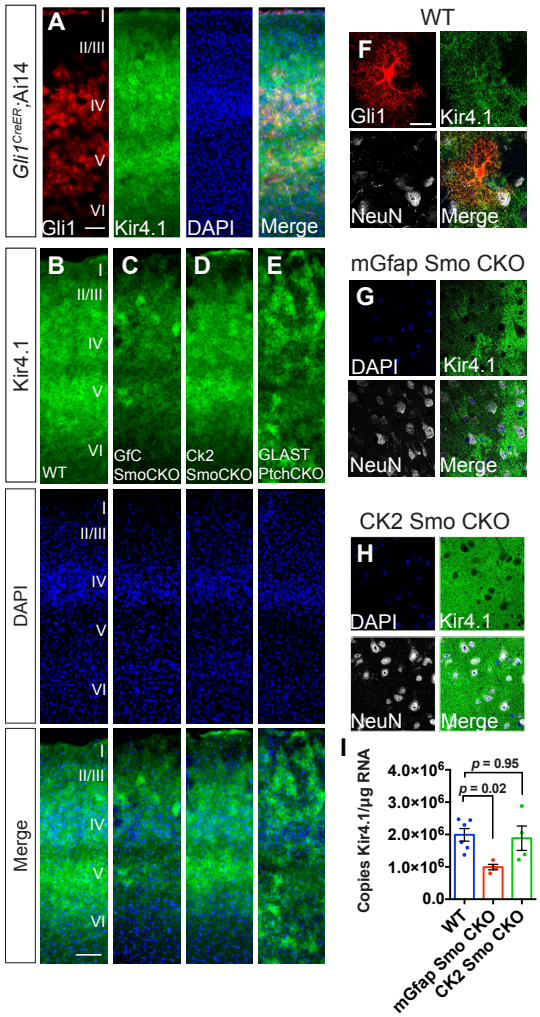

Figure 4: Shh signaling regulates Kir4.1 expression in the cortex. (A) Fluorescence micrographs showing the distribution of Gli1 astrocytes (A, red) and Kir4.1 (A, green) in the cortex of an adult *Gli1Cre*^{ER};Ai14 mouse counterstained with DAPI (A, blue). **(B-E)** Immunofluorescence for Kir4.1 in the cortex of adult WT (B), mGfap Smo CKO (C), CK2 Smo CKO (D) and GLAST Ptch CKO mice (E). Scale bar, 125 µm. **(F-G)** Confocal images of Gli1 (F, red) Kir4.1 (green) and NeuN (white) from adult WT (F), mGfap SmoCKO (G), or CK2 SmoCKO (H) mice. Scale bar, 25 µm. **(I)** Gene expression levels in the cortex of Kir4.1 from WT (*n* = 6 animals) and mGfap Smo CKO or CK2 Smo CKO mice (*n* = 4 each). Data points represent individual animals and bar graphs represent mean value ± SEM. Statistical significance was assessed by one-way ANOVA with Tukey's test for multiple comparisons. Significance stated on the graph is compared to WT.

In the mature cerebellum, Shh signaling between Purkinje neurons and Bergmann glia regulates expression of the glial specific, inward-rectifying K^+ channel, Kir4.1 [19]. In the cortex, the distribution of Kir4.1 exhibits a laminar pattern similar to that of Gli1 astrocytes, such that expression is enriched in layers IV and Vb, and reduced in layer Va (**Figure 4**). High resolution, confocal analysis showed that Kir4.1 is localized in the processes of Gli1 astrocytes (**Figure 4**). Kir4.1 expression is localized to astrocytic endfeet and is found surrounding neuronal somata in the spinal cord and brain [39–41]. In WT mice, expression of Kir4.1 surrounded many NeuN-positive neuronal somata in layer V (**Figure 4).** In mGFAP Smo CKO mice, however, there was a pronounced reduction in the expression of Kir4.1 throughout the cortex, and peri-somal Kir4.1 expression was severely diminished (**Figure 4**). In order to quantify expression levels of Kir4.1, we measured transcript abundance in the cortex of mGFAP Smo CKO mice and WT controls by droplet digital PCR (ddPCR). In mGFAP Smo CKO mice, there was a 50% reduction in *Kir4.1* transcripts compared to WT controls ($1.99 \times 10^6 \pm 1.93 \times 10^5$ copies/µl and $9.92 \times 10^5 \pm 8.49 \times 10^4$ copies/µl in WT [*n* = 6 mice] and mGFAP Smo CKO [*n* = 4 mice], respectively, $p = 0.02$). There was no difference in *Kir4.1* expression in CK2 Smo CKO mice compared to WT ($1.88 \times 10^6 \pm 3.77 \times 10^5$ copies/µl, $p = 0.95$, *n* = 4 mice;

Figure 4), suggesting that downregulation of *Kir4.1* is due to astrocyte-specific, and not neuronal, disruption of Shh signaling. Conversely, GLAST-CreER-mediated deletion of the Shh receptor *Ptch1*, a negative regulator of Shh signaling, dramatically upregulated Kir4.1 expression in the cortex (Ptch CKO; **Figure 4**). Kir4.1 expression is associated with glutamate uptake both *in vitro* and *in vivo* [42–44]. We therefore measured expression levels of the astrocyte-specific glutamate transporters *GLAST* and *GLT1*. There was no difference in expression of these genes in mGFAP Smo CKO mice compared to WT (*GLT1*: $1.08 \times 10^7 \pm 6.6 \times 10^5$ copies/µl and $9.58 \times 10^6 \pm 2.1 \times 10^5$ copies/µl in WT and mGFAP Smo CKO, respectively, p = 0.15, *n* = 3 animals per genotype; *GLAST*: $7.4 \times 10^6 \pm 4.4 \times 10^5$ copies/µl and $6.7 \times 10^6 \pm 6.5 \times 10^5$ copies/µl in WT and mGFAP Smo CKO, respectively, *p* = 0.41, *n* = 3 animals per genotype; **Figure 4 – figure supplement 1**). It should be noted that Kir4.1 was not restricted to Gli1 astrocytes in layers IV and Vb. Nevertheless, single transcript quantification of Kir4.1 transcripts in mGFAP Smo CKO show a pronounced reduction, suggesting that Kir4.1 expression in cortical astrocytes is regulated, in part, by Shh signaling.

Neurons exhibit hyperexcitability in mGFAP Smo CKO mice

Astrocytes play critical roles in buffering K^+ in the extracellular space through Kir4.1, and loss of Kir4.1 produces disturbances in neuronal firing properties [39,40,43–47]. To examine whether neurons in mGFAP Smo CKO mice exhibit disruptions in physiological activity, we performed whole-cell patch clamp recordings and first examined action potential firing and membrane properties of layer V pyramidal neurons from coronal brain slices at P21. Using current clamp, we recorded action potential spikes per injected current at multiple step currents

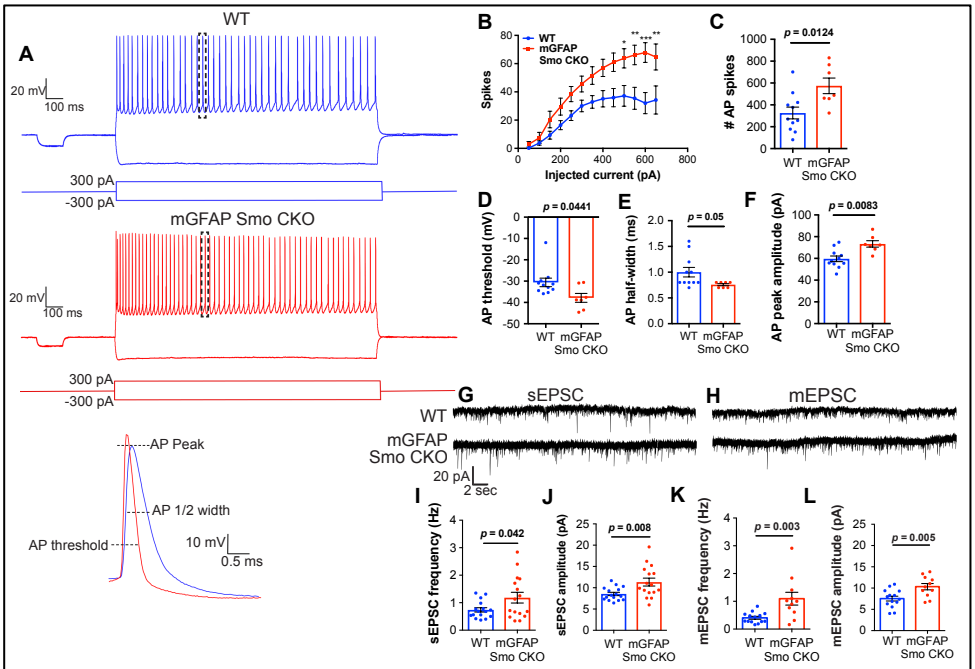

Figure 5. mGFAP Smo CKO neurons exhibit a significant increase in excitability and synaptic transmission. (A) Example traces of action potentials from layer V pyramidal neurons in WT and mGFAP Smo CKO mice at P21. Samples of action potential spikes (dashed lines, lower panel) describe AP threshold, AP peak amplitude, and AP ½ width of pyramidal neuron. **(B)** Line graph displays relationship between action potential spike numbers (y-axis) versus current injection; mGFAP Smo CKO neurons exhibit an increase in AP spikes (>500 pA) compared to WT neurons. Statistical signifcance was assessed by two-way ANOVA with Sidak's test for multiple comparisons and stated as mGFAP Smo CKO compared to WT at a given current (n = 11 and 7 cells from WT and mGFAP Smo CKO, respectively). **(C-F)** Bar graphs describe an increase in total AP spike numbers (C), reduction in AP threshold (mV) (D), reduction in AP 1/2 width (E), and increase in AP peak amplitude (pA) (F) in mGFAP Smo CKO neurons. **(E)** Example traces of sEPSCs from layer V pyramidal neurons recorded in the presence of picrotoxin from WT and mGFAP Smo CKO mice at P21. **(F)** Summary graphs of sEPSC frequency and amplitude (n = 14 and 11 cells from WT and mGFAP Smo CKO animals, respectively). **(G)** Example traces of mEPSCs from layer V pyramidal neurons recorded in the presence of picrotoxin and TTX. **(H)** Summary graphs of sEPSC frequency and amplitude (n = 16 cells per genotype). mGFAP Smo CKO neurons exhibit increases in both frequency and amplitude in sEPSCs and mEPSCs recordings. Statistical significance was assessed by unpaired Student's t-test. All data are from at least 3 animals per genotype.

398 from -300 pA to +650 pA. Our
399 results revealed a significant
400 increase in spike numbers
401 with high current injections
402 (>500 pA) and total overall
403 spikes in mGFAP Smo CKO
404 animals compared to WT
405 control (326 ± 54 and 574 ± 71
406 spikes in WT [*n* = 11 cells from
407 4 animals] and mGFAP Smo
408 CKO [*n* = 7 cells cells from 3 animals], respectively, *p* = 0.01; **Figure 5**). We also measured other
409 membrane properties, including input resistance, resting membrane potential and tau, and found no
410 significant difference between mGFAP Smo CKO and WT neurons (**Figure 5 – figure supplement 1**).
411 However, we observed a significant decrease in action potential threshold (-30.6 ± 2.0 and -37.9 ± 2.0
412 mV in WT and mGFAP Smo CKO, respectively, *p* = 0.0441), accompanied by an increase in action
413 potential amplitude (59.6 ± 2.6 and 73.3 ± 3.0 pA in WT and mGFAP Smo CKO, respectively, *p* = 0.0083),
414 and a trending decrease in action potential ½ width (1.0 ± 0.92 and 0.76 ± 0.02 ms in WT and mGFAP
415 Smo CKO, respectively, *p* = 0.05) in mGFAP Smo CKO neurons, consistent with an increase in neuron
416 excitability (**Figure 5**). Together, these results suggest mGFAP Smo CKO neurons exhibit an increase in
417 neuronal excitability consistent with excess extracellular K^+.

	WT (n = 11 cells)	mGFAP Smo CKO (n = 7 cells)	*P* value
Input resistance (MΩ)	130.6 ± 21.52	97.93 ± 11.49	0.15
Resting membrane potential (mV)	-59.37 ± 2.059	-63.73 ± 3.248	0.25
Tau (ms)	11.76 ± 0.71	11.75 ± 1.398	0.79

Figure 5 – figure supplement 1. Membrane properties of mGFAP Smo CKO layer V pyramidal neurons. There is a significant decrease in input resistance (MΩ) in mGFAP Smo CKO neurons compared to WT neurons. No significant differences were observed in resting membrane potential (mV), rheobase (pA), and tau (ms) in mGFAP Smo CKO neurons. Statistical significance was assessed by Mann-Whitney U test (input resistance and tau) and unpaired Student's t-test (resting membrane potential).

418 To examine excitatory synaptic transmission, we recorded spontaneous and miniature excitatory
419 postsynaptic currents (sEPSCs and mEPSCs) in layer V pyramidal neurons. We found an increase in both
420 the frequency (0.74 ± 0.08 and 1.18 ± 0.19 Hz in WT and mGFAP Smo CKO, respectively, *p* = 0.042) and
421 amplitude (8.54 ± 0.38 and 11.33 ± 0.91 pA in WT and mGFAP Smo CKO, respectively, *p* = 0.008) of
422 sEPSCs in slices from mGFAP Smo CKO mice compared to WT control slices (*n* = 16 cells from 4 animals
423 per genotype; **Figure 5**). Furthermore, we observed an increase in the frequency (0.40 ± 0.05 and 1.10 ±
424 0.23 Hz in WT and mGFAP Smo CKO, respectively, *p* = 0.003) and amplitude (7.54 ± 0.57 and 10.34 ± 0.74
425 pA in WT and mGFAP Smo CKO, respectively, *p* = 0.005) in mEPSCs in the presence of tetrodotoxin (TTX),
426 indicating an increase in postsynaptic response of neurons in mGFAP Smo CKO mice (*n* = 14 and 11 cells
427 from WT and mGFAP Smo CKO, respectively, 4 animals per genotype; **Figure 5**). These data suggest that
428 loss of Shh activity in astrocytes produces disturbances in both pre and postsynaptic activity. Moreover,
429 these data suggest that astrocytes modulate both neuronal excitability and excitatory synaptic
430 transmission in a Shh-dependent manner.

431 Selective disruption of Shh signaling in astrocytes produces mild reactive gliosis

432 We previously demonstrated that cortical astrocytes in mGFAP Smo CKO mice upregulate GFAP
433 expression and exhibit cellular hypertrophy, two classic hallmarks of reactive astrogliosis [15]. Astrocytes
434 exhibiting these features were broadly distributed across cortical layers (**Figure 6**), in contrast to the
435 distribution of Gli1 astrocytes which are found predominantly in layers IV and V. In addition to
436 upregulation of GFAP, astrocytes in mGFAP Smo CKO mice show dramatic changes in morphological
437 structure. Sholl analysis revealed no difference in the number of primary branches in mGFAP Smo CKO

mice compared to WT controls (7.2 and 7.5 branches, WT and mGFAP Smo CKO, respectively; n = 9 cells from 3 animals per genotype). However, astrocytes from mGFAP Smo CKO animals did show an increase in the number of higher order branches, the length of the longest tree (136.6 ± 17 and 212.1 ± 28 µm for WT and mGFAP Smo CKO, respectively, p = 0.035), and the total length of all processes (397 ± 66 and 674 ± 91 µm for WT and mGFAP Smo CKO, respectively, p = 0.025) compared to WT controls (**Figure 6**). Consistent with this, there was a significant increase in the number of branches intersecting concentric shells at various distances from the soma (**Figure 6**). Notably, in CK2 Smo CKO mice, GFAP staining in the cortex was indistinguishable from WT controls (**Figure 6 – figure supplement 1**), suggesting that astrocytes exhibit dramatic changes in morphological structure following astrocytic, but not neuronal, disruption of Shh signaling. Such changes in morphology are consistent with mild reactive gliosis, a complex cellular response of astrocytes to disturbances in physiological homeostasis [48]. Notably, the distribution of reactive astrocytes in mGFAP Smo CKO mice is broader than that defined by Gli1 expression, arguing against the idea that Shh signaling regulates the intrinsic state of astrocytes. Rather, reactive gliosis may instead reflect a cellular response to the mild, but persistent, aberrations in neuronal activity observed in mGFAP Smo CKO mice.

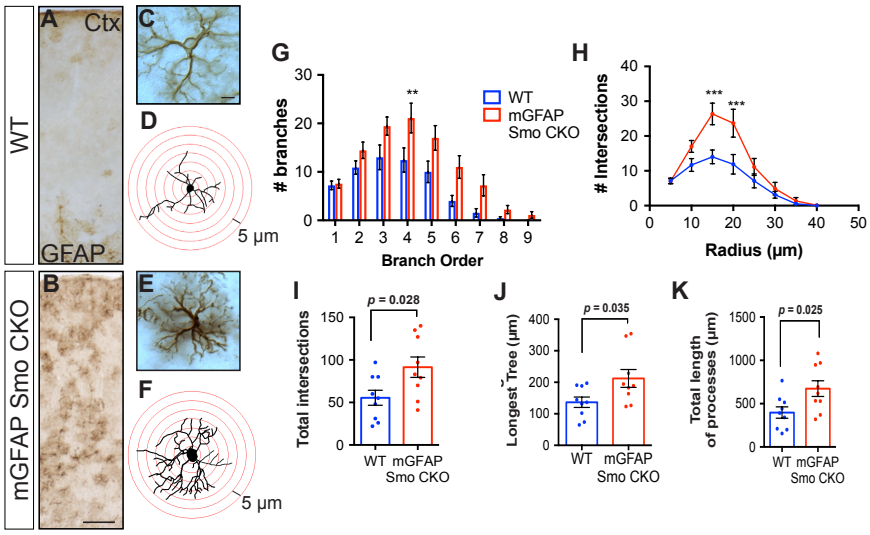

Figure 6: Disruption of Shh signaling in astrocytes results in widespread reactive changes in morphology. (A & B) Brightfield immunohistochemistry reveals a reactive upregulation of GFAP across cortical layers in mGFAP Smo CKO astrocytes. Scale bar, 125 µm. **(C & E)** Representative high-magnification images of both WT (C) and mGFAP Smo CKO (E) astrocytes are shown. Scale bar, 10 µm. **(D & F)** Representative traces of GFAP expression from WT (D) and mGFAP Smo CKO (F) cortical astrocytes. **(G & H)** Sholl analysis shows significant increases in complexity of mGFAP Smo CKO astrocytes compared to WT controls. Statistical significance was assessed by one-way ANOVA with Bonferroni's for multiple comparisons. **(I-K)** Quantification of various morphological features of traced astrocytes. Statistical analysis performed by one-way ANOVA (G & H) and unpaired Student's t-test (I-K). Data points represent individual cells. Graphs represent mean value ± SEM. n = 3 animals per genotype.

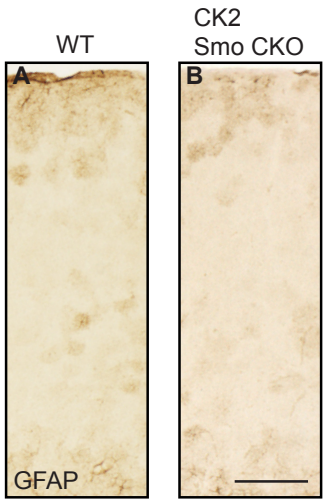

Figure 6 – figure supplement 1: Reactive gliosis does not occur when neuronal Shh signaling is disrupted. Brightfield immunohistochemistry for GFAP in *CamKIIa;Smo*$^{fl/fl}$ animals (B) and littermate controls (A) does not reveal mild reactive gliosis. Scale bar, 250 µm.

DISCUSSION

In this study, we demonstrate that refinement of neural circuits during postnatal development requires neuron-astrocyte signaling mediated by Shh signaling. Our data show that Gli1 astrocytes are enriched in deep cortical layers with a relative paucity in upper cortical layers.

478 Selective disruption of Shh signaling in astrocytes leads to an overabundance of spines on the apical
479 dendrites of layer V, but not layer II/III, cortical neurons. The overabundance of spines emerges during
480 postnatal development, continues into adulthood and is accompanied by a reduction in dynamic
481 turnover. mGFAP Smo CKO mice exhibit a pronounced reduction in Kir4.1 and a concomitant increase in
482 intrinsic neuronal excitability, consistent with a deficit in astrocyte-mediated K^+ buffering. Finally, we
483 show that cortical astrocytes exhibit dramatic changes in morphology and GFAP expression, a
484 phenotype consistent with reactive gliosis. Taken together, these data suggest that local neuron-
485 astrocyte interactions mediated by Shh signaling facilitate modulation of neuronal activity that regulates
486 synaptic remodeling during postnatal development.

487 In the postnatal cortex, Shh signaling from layer V neurons mediates synaptic connectivity with their
488 layer II/III presynaptic partners [14]. Here, we show that, in addition to neuronal Shh signaling, Shh
489 signaling in astrocytes is required for the establishment and maintenance of cortical circuits. This is
490 supported by two key observations in our study. First, we find that in mGFAP Smo CKO mice, apical
491 dendrites of cortical neurons exhibit an increase in spine density that emerges during postnatal
492 development and persists into adulthood. Importantly, genetic deletion of *Smo* in mature neurons
493 instead of astrocytes failed to show any differences in spine density, pointing to a specific role for Shh
494 signaling in astrocyte regulation of synaptic connectivity. Interestingly, deletion of Shh ligand using an
495 EmxCre driver produces a reduction in spine density of basal dendrites [14], whereas we found no
496 difference in basal dendrite spine density, suggesting that Shh acts in distinct, cell type-specific ways to
497 regulate synaptic connectivity of local cortical circuits. Indeed, whereas astrocytes express Gli1, neurons
498 do not [15], indicating differential transduction of Shh through canonical and non-canonical, Gli-
499 independent pathways, respectively, in different cell types. Second, our data show fewer filopodia in
500 juvenile mGFAP Smo CKO mice compared to WT controls along with a concomitant increase in spine
501 stability. In the adult, spines continue to show deficits in dynamic turnover, demonstrating long-term
502 impairments in structural plasticity. This suggests that Shh signaling is required not only for identifying
503 appropriate synaptic partners during development, but it also plays an important role in mediating
504 synaptic plasticity.

505 We previously demonstrated that Gli1 expression is restricted to a subpopulation of cortical astrocytes
506 [15]. Here, we extend these findings and demonstrate that the distribution of Gli1 astrocytes in the cortex
507 is not uniform across cortical layers, but rather, occurs in a laminar-specific fashion. Cortical layers have
508 been historically defined by neuronal populations and their specific functional properties and
509 connectivity. However, emerging evidence suggests that astrocytes also exhibit cortical lamination
510 patterns based on distinct gene expression profiles [49]. Our data show that Gli1 astrocytes are enriched
511 in layers IV and V with a relatively sparse distribution in layer II/III. Interestingly, in the visual cortex, the
512 BMP antagonist, chordin-like 1 (Chrdl1) is preferentially enriched in upper layer cortical astrocytes [8],
513 suggesting that Gli1 and Chrdl1 may identify two distinct, but regionally complementary, astrocyte
514 populations. Alternatively, Shh signaling may actively repress Chrdl1 expression in deep layer
515 astrocytes. Notably, our observation that Gli1 astrocytes only comprise a fraction of astrocytes in layers
516 IV and V suggests that, in addition to the laminar-specific distribution of these cells, there may be
517 additional heterogeneity of astrocytes even with a given cortical layer. Whether and how the laminar

518 distribution of astrocytes with distinct gene expression profiles confers functional specialization is not
519 well understood and requires further study.

520 Interestingly, we observed that the disturbances in synaptic organization of cortical neurons in mGFAP
521 Smo CKO mice occurs selectively in apical dendrites of layer V, but not layer II/III, neurons. Since apical
522 dendrites of layer V neurons traverse through layer II/III, this suggests that Shh-dependent regulation of
523 synaptic refinement is not mediated by direct interaction between Gli1 astrocytes and synapses. One
524 possibility is that Gli1 astrocytes interact with neuronal soma in layer V and effectively modulate their
525 excitability by providing peri-somatic buffering of extracellular K^+. Indeed, a recent study demonstrated
526 that Kir4.1 surrounds neuronal soma in the lateral habenula and regulates their firing properties [40].
527 Astrocytes play essential roles in buffering extracellular K^+ through Kir4.1, and several studies
528 demonstrate that loss of function of Kir4.1 inhibits K^+ uptake and increases neuronal excitability [43,44,50].
529 The establishment of appropriate synapse number and connectivity are tightly regulated processes that
530 are profoundly shaped by experience or activity [33,51]. Our observation that mGFAP Smo CKO mice show
531 a pronounced reduction in Kir4.1 expression accompanied by increases in spontaneous neuronal activity
532 and excitability suggests that the activity-dependent processes that govern the refinement of excess
533 synapses are impaired.

534 Aberrant synaptic number and organization characterize a number of neurodevelopmental disorders [1].
535 In addition, remodeling of spines following insult or disease is essential for preserving or restoring
536 function. Here, we demonstrate that Shh signaling mediates neuron-astrocyte interactions that are
537 necessary for refining developing neural circuits. The deficits in synaptic organization observed in
538 mGFAP Smo CKO mice persist for the life of the animal. These deficits are not limited to synapse
539 number but also include lower rates of spine turnover, suggesting long-lasting deficits in structural
540 plasticity. Together with the observation that Shh guides local synaptic connectivity of cortical neurons
541 [14], these studies reveal that Shh signaling exerts considerable influence on the establishment and
542 maintenance of cortical circuits. Further, these results reveal a specific role for astrocytes in mediating
543 synaptic connectivity of local cortical circuits. These results point to Shh signaling in astrocytes as a
544 potential molecular and cellular target for developing novel strategies to overcome aberrant synaptic
545 connectivity.

546 METHODS

547 *Animals*

548 All experiments were approved by Drexel University's Institutional Animal Care and Use Committee and
549 were conducted according to approved protocols. We used the following strains of transgenic mice on
550 the C57BL/6 background: *Gli1*$^{CreER/+}$ [12], Ai14 [52], *Smo*$^{fl/fl}$ [53], *mGFAP-Cre*[20], *CaMKIIa-Cre*[54] and *Thy1-GFPm*[24].
551 Mice of either sex were included in these studies.

552 *Immunohistochemistry*

553 Mice were deeply anesthetized by intraperitoneal injection of ketamine/xylazine/acepromazine.
554 Animals were then transcardially injected with 100 units heparin and perfused with phosphate-buffered
555 saline (PBS) followed by 4% paraformaldehyde (PFA, Sigma-Aldrich, St. Louis, MO). Brains were fixed

556 overnight at 4°C and then transferred to 30% sucrose for at least 48 hours or until sectioned. Brains
557 were cryosectioned (Leica CM3050S, Wetzlar, Germany) and collected in 40 µm sections. Sections were
558 stored in 0.1M Tris-buffered saline (TBS) with 0.05% sodium azide at 4°C. Immunohistochemistry was
559 performed using the following primary antibodies: rabbit anti-GFP (AB3080; Millipore, Burlington, MA),
560 rabbit anti-Kir4.1 (AB5818; Millipore), rabbit anti-GFAP (Z033429-2; Agilent, Santa Clara, CA), mouse
561 anti-NeuN (MAB377; Millipore), rabbit anti-RFP (PM005; MBL International, Woburn, MA), rat anti-Ctip2
562 (ab18465; Abcam, Cambridge, UK), sheep anti-CAII (AHP206; Bio-Rad), rabbit anti-S100β (Z0311,
563 Agilent), and rabbit anti-Olig2 (AB9610; Millipore). Sections were washed three times in 0.1M TBS at
564 room temperature (10 minutes/wash). Sections were then blocked in 10% Normal Serum with 0.5%
565 Triton-X (Sigma-Aldrich) for one hour at room temperature and incubated with primary antibody in 0.5%
566 Triton-X at 4°C overnight. For fluorescent immunohistochemistry, sections were rinsed the following day
567 in 0.1M TBS and incubated in Alexafluor-conjugated secondary antibodies with 10% Normal Serum and
568 0.1M TBS and incubated at room temperature for two hours. The sections were then rinsed in 0.1 TBS
569 and incubated in DAPI (1:50,000; Life Technologies, Carlsbad, CA) for 15 minutes. Sections were rinsed
570 again in 0.1M TBS and mounted onto microscope slides (Fisherbrand, Waltham, MA) and coverslipped
571 using ProLong Gold Antifade Mountant (Invitrogen, Carlsbad, CA) and Fisherfinest Premium Cover Glass.
572 For brightfield immunohistochemistry, sections were rinsed as previously described but were incubated
573 with biotinylated secondary antibodies against the primary antibody species (Vector Laboratories,
574 Burlingame, CA) for one hour. Sections were then placed in Avitin-Biotin Complex solution (Vector) for
575 one hour and visualized using 3,3'-diaminobenzidine (DAB Peroxidase Substrate Kit, Vector). Sections
576 were then mounted onto slides and coverslipped with DPX Mountant (Fisher).

577 *Quantification of dendritic spine density*

578 Neurons were traced using Neurolucida 11 (MicroBrightField Biosciences, Williston, VT) and individual
579 spines were marked. Apical dendrites of layer V neurons were counted from ~100 µm below the primary
580 bifurcation through the apical tuft. Apical dendrites of layer II/III cells were analyzed just below the
581 primary bifurcation through the apical tuft. Basal dendrites were analyzed beginning ~50 µm from the
582 soma through the end of the processes. CA1 hippocampal neurons were analyzed from just below the
583 primary bifurcation through the apical tuft. All analysis was performed on an upright Zeiss microscope
584 using a 63x oil objective.

585 *Cranial window*

586 Cranial window surgeries were adapted from a published protocol[34]. Immediately prior to each surgery,
587 mice received a subcutaneous injection of carprofen (Rimadyl, 5 mg/kg), and a follow-up injection was
588 given 24 hours after surgery. Mice were deeply anesthetized with isoflurane (5%) in an induction
589 chamber, and then transferred to a stereotaxic apparatus where they inhaled 1.5% isoflurane
590 continuously for the duration of the surgery. The scalp was then removed and a metal bar (~1 cm long)
591 with threadings for screws was affixed to the skull, using superglue and dental acrylic to form a head
592 post that sealed off the skin while leaving the right parietal bone exposed. After allowing 24 hours for
593 the glue and acrylic to set, the mouse was returned to the stereotaxic apparatus and head-fixed using
594 the headpost. A circular craniotomy ~3 mm in diameter and centered 2.5 mm lateral and posterior to

595 bregma was performed. The exposed dura was treated with saline-soaked gel foam until any minor
596 bleeding ceased. Finally, a 3 mm glass coverslip was gently pressed onto the dura and sealed in place
597 using superglue and dental acrylic. Adult mice were allowed at least 1 week for recovery. To mitigate the
598 tendency of rapid bone growth to destabilize the windows at younger ages, juvenile mice were allowed
599 24 hours to recover.

600 *Two-photon imaging*

601 A commercial two-photon microscope (Bruker, Billerica, MA) with a tunable Ti:Sapphire laser (Coherent,
602 Santa Clara, CA) was used for all experiments. The laser was set to 920 nm and power was tuned on the
603 sample as necessary to obtain consistently high-quality images without damaging the tissue. Mice were
604 head-fixed and anesthetized with continuous isoflurane (1-1.5%) during imaging. Under a 20X water
605 immersion objective, GFP-expressing neurons were identified visually and then imaged down to the cell
606 body to determine layer. From the apical dendrite tuft, individual dendrite segments that projected
607 primarily along the xy-plane were selected for analysis, and z-stacks (0.5 µm step size) were collected.
608 To track individual dendrites, repeated imaging was generally performed on the following schedule (in
609 days, relative to first imaging session): 0, 1, 2, 7, 14, 21, 28, 42. Some data from studies using other
610 schedules were also included. For juvenile mice, this schedule was: 0, 1, 2.

611 *Analysis of structural plasticity*

612 Initial measures of structural plasticity were determined by side-by-side manual comparison of two z-
613 stacks across a fixed time-interval (7 days for adults, 2 days for juvenile). These comparisons were
614 conducted by trained observers blinded to mouse genotype. Long, thin protrusions lacking a bulbous
615 head were identified as filopodia, and any other prominent dendritic protrusion that extended > 0.4 µm
616 from the shaft was counted as a spine. The filopodial fraction was calculated as the proportion of all
617 analyzed features present at the first imaging timepoint that were identified as filopodia. The position
618 and dynamic status (stable/eliminated/formed) of each spine was recorded using ImageJ's CellCounter
619 plugin. Each neuron's turnover ratio was calculated as:

620 $$TO = (N_{elim} + N_{form})/(N_{elim} + N_{form} + 2N_{stable})$$

621

622 For longitudinal studies, the dendritic features identified in our initial ImageJ-based analysis were
623 imported into MATLAB (Mathworks, Natick, MA) and manually tracked across all imaged time-points
624 using custom-written software. Spines that were observed consistently across all time point were
625 classified as stable. Spines that disappeared at some time point and were observed again in a
626 subsequent time point were classified as recurrent. Spines that disappeared and never reappeared were
627 classified as transient. To compare long-term dynamics between WT and mGFAP Smo CKO mice, we
628 examined the survival curves, S(t), for each mouse, where:

629 S(t) = # of spines consistently present to time point t / # of spines initially observed

630 Survival curves for each mouse were pooled by genotype and fit to a single-phase exponential decay
631 model:

632 $$S(t) = S_p + S_i*\exp(-t/\tau)$$

633 where S_p and S_i represent the relative fractions of permanent and impermanent spines respectively and
634 τ is the characteristic lifespan of impermanent spines. Fitting and statistical comparison of survival data
635 was performed with PRISM 6 (GraphPad, San Diego, CA) software.
636
637 *Transcript Quantification*
638 Mice were deeply anesthetized by intraperitoneal injection of ketamine/xylazine/acepromezine before
639 rapid decapitation. Cortices were dissected into TRIzol reagent (Thermo-Fisher, Waltham, MA) and RNA
640 was extracted according to the standard protocol. RNA was then purified with an RNeasy Micro Kit
641 (Qiagen, Hilden, Germany) and subsequently reverse transcribed to cDNA using the High-Capacity cDNA
642 Reverse Transcription Kit (Thermo-Fisher). Droplet digital PCR (ddPCR) was performed with the QX200
643 Droplet Digital PCR System using Evagreen Supermix (Bio-Rad, Hercules, CA). Alternatively, for *Megf10*
644 and *Mertk*, qPCR was performed with the CFX96 Touch Real-Time PCR Detection System (Bio-Rad) using
645 PowerUp SYBR Green Master Mix (Thermo-Fisher). PrimePCR ddPCR Expression EvaGreen Assay (Bio-
646 Rad) was used for *Gapdh* primers; all other primers were designed using NCBI Primer-BLAST as follows:
647 *Kir4.1* F, GCTGCCCCGCGATTTATCAG; *Kir4.1* R, AGCGACCGACGTCATCTTGG; *GLAST* F,
648 TCCTCTACTTCCTGGTAACCC; *GLAST* R, TCCACACCATTGTTCTCTTCC; *Glt1* F, CATCAACAGAGGGTGCCAAC;
649 *Glt1* R, CACACTGCTCCCAGGATGAC; *Megf10* F, CTCACTGCTCTGTCACTGGGTG; *Megf10* R,
650 GGTAGCTGATTCTGTGCCGTGT; *Mertk* F, AAACTGCATGTTGCGGGATGAC; *Mertk* R,
651 TCCCACATGGTCACGCCAAA. ddPCR absolute quantification of targets was calculated using Quantasoft
652 Version 1.7 software (Bio-Rad). Samples were run in triplicate, and *Gapdh* was quantified for each
653 sample as a loading control with no difference detected between sample groups.

654 *Slice electrophysiology*

655 Mice aged P21 were anesthetized with intraperitoneal injection of euthasol (0.2 ml/kg) and brains were
656 rapidly removed. 300 µm coronal slices were cut using a vibratome tissue slicer (Leica) and transferred
657 to a holding chamber, submerged in oxygenated artificial cerebrospinal fluid (ACSF, in mM: 124 NaCl, 2.5
658 KCl, 1.25 NaH_2PO_4, 2 $CaCl_2$, 1 $MgSO_4$, 26 $NaHCO_3$, and 10 dextrose, pH 7.4) at 36°C for 1 hour and then
659 maintained at room temperature. Individual slices containing the barrel cortex were placed into a
660 recording chamber immersed in oxygenated ACSF mounted on an Olympus upright microscope (BX51).
661 Neurons were visualized with infrared differential interference video microscopy.
662
663 Whole-cell current clamp was used to record action potentials from layer V pyramidal cells using patch
664 electrodes with an open tip resistance of 7–10 MΩ. Patch electrodes were filled with potassium
665 gluconate internal solution (in mM): 120 potassium gluconate, 20 KCl, 4 ATP-Na, 0.3 Na_2GTP, 5 Na-
666 phosphocreatine, 0.1 EGTA, 10 HEPES, pH 7.3, 305 mosmol/l) and action potential responses were
667 measured in response to various step currents from -300 pA to +650 pA with 50 pA increments. Action
668 potentials were described as spike numbers per depolarized current injections. The resting membrane
669 potential, input resistance, action potential (AP) threshold, AP half-width, and peak AP amplitude were
670 also measured.
671
672 Whole-cell voltage-clamp recordings were obtained from layer V pyramidal cells using patch electrodes
673 with Cs^+-containing solution (in mM): 120 Cs-gluconate, 5 lidocaine, 6 $CaCl_2$, 1 Na_2ATP, 0.3 Na_2GTP, and

674 10 HEPES (pH 7.3 adjusted by CsOH). To record spontaneous excitatory postsynaptic currents (sEPSCs),
675 cells were held at a membrane potential of -70mV in the presence of $GABA_A$ receptor antagonist
676 picrotoxin (PTX; 100 µM, Sigma-Aldrich) and recorded for 5 minutes. Miniature EPSCs (mEPSCs) were
677 then recorded for an additional 5 minutes in the presence of both picrotoxin and tetrodotoxin (TTX, 0.5
678 µM, Hello Bio, Princeton, NJ). All recordings were conducted with Axon MultiClamp 700B amplifier
679 (Molecular Devices, San Jose, CA). The sEPSCs and mEPSCs frequency and amplitudes were measured by
680 averaging 5 sweeps from the onset of recording with Clampfit 9.2 software (Molecular Devices). The
681 s/mEPSCs were detected and characterized using a sample template for the 5-minute data period. Based
682 upon the selected sample template, the frequency (number of event detections) and amplitude of
683 events were measured using a threshold set in Clampfit.

684 *Statistical Analyses*

685 Statistical analyses used for various datasets are indicated both in the figure legends and in the text.
686 Prism 6 software (GraphPad) was used for all analyses and to generate graphs.

687 # REFERENCES

688 1. Penzes, P., Cahill, M. E., Jones, K. A., VanLeeuwen, J.-E. & Woolfrey, K. M. Dendritic spine
689 pathology in neuropsychiatric disorders. *Nat. Neurosci.* **14**, 285–293 (2011). DOI:
690 10.1038/nn.2741

691 2. Allen, N. J. & Eroglu, C. Cell Biology of Astrocyte-Synapse Interactions. *Neuron* **96**, 697–708
692 (2017). DOI: 10.1016/j.neuron.2017.09.056

693 3. Adamsky, A., Kol, A., Groysman, M., London, M., Kreisel, T., Doron, A., Ozeri-Engelhard, N.,
694 Melcer, T., Refaeli, R., Horn, H., Regev, L. & Goshen, I. Astrocytic Activation Generates De Novo
695 Neuronal Potentiation and Memory Enhancement. *Cell* **174**, 59–71 (2018). DOI:
696 10.1016/j.cell.2018.05.002

697 4. Risher, W. C., Patel, S., Kim, I. H. wan, Uezu, A., Bhagat, S., Wilton, D. K., Pilaz, L. J., Singh
698 Alvarado, J., Calhan, O. Y., Silver, D. L., Stevens, B., Calakos, N., Soderling, S. H. & Eroglu, C.
699 Astrocytes refine cortical connectivity at dendritic spines. *Elife* **3**, 166–175 (2014). DOI:
700 10.7554/eLife.04047

701 5. Allen, N. J., Bennett, M. L., Foo, L. C., Wang, G. X., Chakraborty, C., Smith, S. J. & Barres, B. A.
702 Astrocyte glypicans 4 and 6 promote formation of excitatory synapses via GluA1 AMPA receptors.
703 *Nature* **486**, 410–414 (2012). DOI: 10.1038/nature11059

704 6. Kucukdereli, H., Allen, N. J., Lee, A. T., Feng, A., Ozlu, M. I., Conatser, L. M., Chakraborty, C.,
705 Workman, G., Weaver, M., Sage, E. H., Barres, B. A. & Eroglu, C. Control of excitatory CNS
706 synaptogenesis by astrocyte-secreted proteins Hevin and SPARC. *Proc. Natl. Acad. Sci. U. S. A.*
707 **108**, E440-9 (2011). DOI: 10.1073/pnas.1104977108

708 7. Christopherson, K. S., Ullian, E. M., Stokes, C., Mullowney, C., Hell, J., Agah, A., Lawler, J., Mosher,
709 D., Bornstein, P. & Barres, B. A. Thrombospondins are astrocyte-secreted proteins that promote
710 CNS synaptogenesis. *Cell* **120**, 421–433 (2005).

711 8. Blanco-Suarez, E., Liu, T.-F., Kopelevich, A. & Allen, N. J. Astrocyte-Secreted Chordin-like 1 Drives
712 Synapse Maturation and Limits Plasticity by Increasing Synaptic GluA2 AMPA Receptors. *Neuron*
713 1–17 (2018). DOI: 10.1016/j.neuron.2018.09.043

714 9. Fuccillo, M., Joyner, A. L. & Fishell, G. Morphogen to mitogen: the multiple roles of hedgehog
715 signalling in vertebrate neural development. *Nat. Rev. Neurosci.* **7**, 772–83 (2006). DOI:
716 10.1038/nrn1990

717 10. Ruiz i Altaba, A., Palma, V. & Dahmane, N. Hedgehog–Gli Signalling and the Growth of the Brain.
718 *Nat. Rev. Neurosci.* **3**, 24–33 (2002). DOI: 10.1038/nrn704

719 11. Traiffort, E., Angot, E. & Ruat, M. Sonic Hedgehog signaling in the mammalian brain. *Journal of*
720 *Neurochemistry* **113**, 576–590 (2010). DOI: 10.1111/j.1471-4159.2010.06642.x

721 12. Ahn, S. & Joyner, A. L. In vivo analysis of quiescent adult neural stem cells responding to Sonic
722 hedgehog. *Nature* **437**, 894–897 (2005). DOI: 10.1038/nature03994

723 13. Ihrie, R. A., Shah, J. K., Harwell, C. C., Levine, J. H., Guinto, C. D., Lezameta, M., Kriegstein, A. R. &
724 Alvarez-Buylla, A. Persistent Sonic Hedgehog Signaling in Adult Brain Determines Neural Stem
725 Cell Positional Identity. *Neuron* **71**, 250–262 (2011). DOI: 10.1016/j.neuron.2011.05.018

726 14. Harwell, C. C., Parker, P. R. L., Gee, S. M., Okada, A., McConnell, S. K., Kreitzer, A. C. & Kriegstein,
727 A. R. Sonic Hedgehog Expression in Corticofugal Projection Neurons Directs Cortical Microcircuit

728 Formation. *Neuron* **73**, 1116–1126 (2012). DOI: 10.1016/j.neuron.2012.02.009

729 15. Garcia, A. D. R., Petrova, R., Eng, L. & Joyner, A. L. Sonic hedgehog regulates discrete populations
730 of astrocytes in the adult mouse forebrain. *J. Neurosci.* **30**, 13597–608 (2010). DOI:
731 10.1523/JNEUROSCI.0830-10.2010

732 16. Garcia, A. D. R., Han, Y.-G., Triplett, J. W., Farmer, W. T., Harwell, C. C. & Ihrie, R. A. The Elegance
733 of Sonic Hedgehog: Emerging Novel Functions for a Classic Morphogen. *J. Neurosci.* **38**, 9338–
734 9345 (2018). DOI: 10.1523/JNEUROSCI.1662-18.2018

735 17. Alvarez, J. I., Dodelet-Devillers, A., Kebir, H., Ifergan, I., Fabre, P. J., Terouz, S., Sabbagh, M.,
736 Wosik, K., Bourbonnière, L., Bernard, M., Van Horssen, J., De Vries, H. E., Charron, F. & Prat, A.
737 The hedgehog pathway promotes blood-brain barrier integrity and CNS immune quiescence.
738 *Science (80-.).* **334**, 1727–1731 (2011). DOI: 10.1126/science.1206936

739 18. Allahyari, R. V., Clark, K. L., Shepard, K. A. & Garcia, A. D. R. Sonic hedgehog signaling is negatively
740 regulated in reactive astrocytes after forebrain stab injury. *Sci. Rep.* **9**, 565 (2019). DOI:
741 10.1038/s41598-018-37555-x

742 19. Farmer, W. T., Abrahamsson, T., Chierzi, S., Lui, C., Zaelzer, C., Jones, E. V, Bally, B. P., Chen, G. G.,
743 Théroux, J.-F., Peng, J., Bourque, C. W., Charron, F., Ernst, C., Sjöström, P. J. & Murai, K. K.
744 Neurons diversify astrocytes in the adult brain through sonic hedgehog signaling. *Science (80-.).*
745 **351**, 849–854 (2016). DOI: 10.1126/science.aab3103

746 20. Garcia, A. D. R., Doan, N. B., Imura, T., Bush, T. G. & Sofroniew, M. V. GFAP-expressing
747 progenitors are the principal source of constitutive neurogenesis in adult mouse forebrain. *Nat.*
748 *Neurosci.* **7**, 1233–1241 (2004). DOI: 10.1038/nn1340

749 21. Petrova, R., Garcia, A. D. R. & Joyner, A. L. Titration of GLI3 Repressor Activity by Sonic Hedgehog
750 Signaling Is Critical for Maintaining Multiple Adult Neural Stem Cell and Astrocyte Functions. *J.*
751 *Neurosci.* **33**, 17490–17505 (2013). DOI: 10.1523/JNEUROSCI.2042-13.2013

752 22. Zhuo, L., Theis, M., Alvarez-Maya, I., Brenner, M., Willecke, K. & Messing, A. hGFAP-cre
753 Transgenic Mice for Manipulation of Glial and Neuronal Function In Vivo With the goal of
754 performing astrocyte-specific modifica-tion of genes in the mouse. (2001). DOI:
755 10.1002/gene.10008

756 23. Nimchinsky, E. A., Sabatini, B. L. & Svoboda, K. Structure and Function of Dendritic Spines. *Annu.*
757 *Rev. Physiol.* **64**, 313–353 (2002). DOI: 10.1146/annurev.physiol.64.081501.160008

758 24. Feng, G., Mellor, R. H., Bernstein, M., Keller-Peck, C., Nguyen, Q. T., Wallace, M., Nerbonne, J. M.,
759 Lichtman, J. W. & Sanes, J. R. Imaging Neuronal Subsets in Transgenic Mice Expressing Multiple
760 Spectral Variants of GFP. *Neuron* **28**, 41–51 (2000). DOI: 10.1016/S0896-6273(00)00084-2

761 25. Zuo, Y., Lin, A., Chang, P. & Gan, W.-B. Development of Long-Term Dendritic Spine Stability in
762 Diverse Regions of Cerebral Cortex. *Neuron* **46**, 181–189 (2005). DOI:
763 10.1016/j.neuron.2005.04.001

764 26. Holtmaat, A., Trachtenberg, J. T., Wilbrecht, L., Shepherd, G. M., Zhang, X., Knott, G. W. &
765 Svoboda, K. Transient and persistent dendritic spines in the neocortex in vivo. *Neuron* **45**, 279–
766 291 (2005). DOI: 10.1016/j.neuron.2005.01.003

767 27. Han, Y. G., Spassky, N., Romaguera-Ros, M., Garcia-Verdugo, J. M., Aguilar, A., Schneider-
768 Maunoury, S. & Alvarez-Buylla, A. Hedgehog signaling and primary cilia are required for the
769 formation of adult neural stem cells. *Nat. Neurosci.* **11**, 277–284 (2008). DOI: 10.1038/nn2059

770 28. Attardo, A., Fitzgerald, J. E. & Schnitzer, M. J. Impermanence of dendritic spines in live adult CA1
771 hippocampus. *Nature* **523**, 592–596 (2015). DOI: 10.1038/nature14467

772 29. Perez-Cruz, C., Nolte, M. W., Van Gaalen, M. M., Rustay, N. R., Termont, A., Tanghe, A., Kirchhoff,
773 F. & Ebert, U. Reduced Spine Density in Specific Regions of CA1 Pyramidal Neurons in Two
774 Transgenic Mouse Models of Alzheimer's Disease. *J. Neurosci.* **31**, 3926–3934 (2011). DOI:
775 10.1523/JNEUROSCI.6142-10.2011

776 30. Lendvai, B., Stern, E. a, Chen, B. & Svoboda, K. Experience-dependent plasticity of dendritic
777 spines in the developing rat barrel cortex in vivo. *Nature* **404**, 876–881 (2000). DOI:
778 10.1038/35009107

779 31. Trachtenberg, J. T., Chen, B. E., Knott, G. W., Feng, G., Sanes, J. R., Welker, E. & Svoboda, K. Long-
780 term in vivo imaging of experience-dependent synaptic plasticity in adult cortex. *Nature* **420**,
781 788–794 (2002). DOI: 10.1038/nature01273

782 32. Holtmaat, A. & Svoboda, K. Experience-dependent structural synaptic plasticity in the
783 mammalian brain. *Nat. Rev. Neurosci.* **10**, 647–658 (2009). DOI: 10.1038/nrn2721

784 33. Zuo, Y., Yang, G., Kwon, E. & Gan, W.-B. Long-term sensory deprivation prevents dendritic spine
785 loss in primary somatosensory cortex. *Nature* **436**, 261–265 (2005). DOI: 10.1038/nature03715

786 34. Holtmaat, A., Bonhoeffer, T., Chow, D. K., Chuckowree, J., De Paola, V., B, H. S., Hübener, M.,
787 Keck, T., Knott, G., Lee, W.-C. A., Mostany, R., Mrsic-Flogel, T. D., Nedivi, E., Portera-Cailliau, C.,
788 Svoboda, K., Trachtenberg, J. T. & Wilbrecht, L. Long-term, high-resolution imaging in the mouse
789 neocortex through a chronic cranial window. *Nat. Protoc.* **4**, 1128–44 (2009). DOI:
790 10.1038/nprot.2009.89

791 35. Ziv, N. E. & Smith, S. J. Evidence for a role of dendritic filopodia in synaptogenesis and spine
792 formation. *Neuron* **17**, 91–102 (1996). DOI: 10.1016/S0896-6273(00)80283-4

793 36. Berry, K. P. & Nedivi, E. Spine Dynamics: Are They All the Same? *Neuron* **96**, 43–55 (2017). DOI:
794 10.1016/j.neuron.2017.08.008

795 37. Grutzendler, J., Kasthuri, N. & Gan, W. B. W.-B. Long-term dendritic spine stability in the adult
796 cortex. *Nature* **420**, 812–816 (2002). DOI: 10.1038/nature01151.1.

797 38. Chung, W.-S., Clarke, L. E., Wang, G. X., Stafford, B. K., Sher, A., Chakraborty, C., Joung, J., Foo, L.
798 C., Thompson, A., Chen, C., Smith, S. J. & Barres, B. a. Astrocytes mediate synapse elimination
799 through MEGF10 and MERTK pathways. *Nature* **504**, 394–400 (2013). DOI: 10.1038/nature12776

800 39. Kelley, K. W., Ben Haim, L., Schirmer, L., Tyzack, G. E., Tolman, M., Miller, J. G., Tsai, H. H., Chang,
801 S. M., Molofsky, A. V., Yang, Y., Patani, R., Lakatos, A., Ullian, E. M. & Rowitch, D. H. Kir4.1-
802 Dependent Astrocyte-Fast Motor Neuron Interactions Are Required for Peak Strength. *Neuron* 1–
803 14 (2018). DOI: 10.1016/j.neuron.2018.03.010

804 40. Cui, Y., Yang, Y., Ni, Z., Dong, Y., Cai, G., Foncelle, A., Ma, S., Sang, K., Tang, S., Li, Y., Shen, Y.,
805 Berry, H., Wu, S. & Hu, H. Astroglial Kir4.1 in the lateral habenula drives neuronal bursts in
806 depression. *Nature* **554**, 323–327 (2018). DOI: 10.1038/nature25752

807 41. Higashi, K., Fujita, A., Inanobe, A., Tanemoto, M., Doi, K., Kubo, T. & Kurachi, Y. An inwardly
808 rectifying K(+) channel, Kir4.1, expressed in astrocytes surrounds synapses and blood vessels in
809 brain. *Am J Physiol Cell Physiol* **281**, C922-31 (2001). DOI: 10.1002/cne.903280405

810 42. Kucheryavykh, Y. V., Kucheryavykh, L. Y., Nichols, C. G., Maldonado, H. M., Baksi, K., Reichenbach,
811 A., Skatchkov, S. N. & Eaton, M. J. Downregulation of Kir4.1 inward rectifying potassium channel

812 subunits by RNAi impairs potassium transfer and glutamate uptake by cultured cortical
813 astrocytes. *Glia* **55**, 274–281 (2007). DOI: 10.1002/glia.20455

814 43. Djukic, B., Casper, K. B., Philpot, B. D., Chin, L. S. & McCarthy, K. D. Conditional knock-out of
815 Kir4.1 leads to glial membrane depolarization, inhibition of potassium and glutamate uptake, and
816 enhanced short-term synaptic potentiation. *J. Neurosci.* **27**, 11354–11365 (2007). DOI:
817 10.1523/jneurosci.0723-07.2007

818 44. Tong, X., Ao, Y., Faas, G. C., Nwaobi, S. E., Xu, J., Haustein, M. D., Anderson, M. A., Mody, I.,
819 Olsen, M. L., Sofroniew, M. V. & Khakh, B. S. Astrocyte Kir4.1 ion channel deficits contribute to
820 neuronal dysfunction in Huntington's disease model mice. *Nat. Neurosci.* **17**, 694–703 (2014).
821 DOI: 10.1038/nn.3691

822 45. Nwaobi, S. E., Cuddapah, V. A., Patterson, K. C., Randolph, A. C. & Olsen, M. L. The role of glial-
823 specific Kir4.1 in normal and pathological states of the CNS. *Acta Neuropathol.* **132**, 1–21 (2016).
824 DOI: 10.1007/s00401-016-1553-1

825 46. Olsen, M. L. & Sontheimer, H. Functional implications for Kir4.1 channels in glial biology: From K +
826 buffering to cell differentiation. *Journal of Neurochemistry* **107**, 589–601 (2008). DOI:
827 10.1111/j.1471-4159.2008.05615.x

828 47. Chever, O., Djukic, B., McCarthy, K. D. & Amzica, F. Implication of Kir4.1 Channel in Excess
829 Potassium Clearance: An In Vivo Study on Anesthetized Glial-Conditional Kir4.1 Knock-Out Mice.
830 *J. Neurosci.* **30**, 15769–15777 (2010). DOI: 10.1523/JNEUROSCI.2078-10.2010

831 48. Sofroniew, M. V. Astrocyte barriers to neurotoxic inflammation. *Nat. Rev. Neurosci.* **16**, 249–263
832 (2015). DOI: 10.1038/nrn3898

833 49. Bayraktar, O. A. et al. Single-cell in situ transcriptomic map of astrocyte cortical layer diversity.
834 *bioRxiv* 432104 (2018). DOI: 10.1101/432104

835 50. Sibille, J., Pannasch, U. & Rouach, N. Astroglial potassium clearance contributes to short-term
836 plasticity of synaptically evoked currents at the tripartite synapse. *J. Physiol.* **592**, 87–102 (2014).
837 DOI: 10.1113/jphysiol.2013.261735

838 51. Yang, G., Pan, F. & Gan, W.-B. Stably maintained dendritic spines are associated with lifelong
839 memories. *Nature* **462**, 920–924 (2009). DOI: 10.1038/nature08577

840 52. Madisen, L., Zwingman, T. A., Sunkin, S. M., Oh, S. W., Zariwala, H. A., Gu, H., Ng, L. L., Palmiter,
841 R. D., Hawrylycz, M. J., Jones, A. R., Lein, E. S. & Zeng, H. A robust and high-throughput Cre
842 reporting and characterization system for the whole mouse brain. *Nat. Neurosci.* **13**, 133–40
843 (2010). DOI: 10.1038/nn.2467

844 53. Long, F., Zhang, X. M., Karp, S., Yang, Y. & McMahon, A. P. Genetic manipulation of hedgehog
845 signaling in the endochondral skeleton reveals a direct role in the regulation of chondrocyte
846 proliferation. *Development* **128**, 5099–108 (2001). DOI: 10.1016/s0092-8674(00)80094-x

847 54. Tsien, J. Z., Chen, D. F., Gerber, D., Tom, C., Mercer, E. H., Anderson, D. J., Mayford, M., Kandel, E.
848 R. & Tonegawa, S. Subregion- and cell type-restricted gene knockout in mouse brain. *Cell* **87**,
849 1317–1326 (1996). DOI: 10.1016/S0092-8674(00)81826-7

850